Research Square

Preprints are preliminary reports that have not undergone peer review.
They should not be considered conclusive, used to inform clinical practice,
or referenced by the media as validated information.

Solid–Solid Catalysis in Sustainable Alloy Synthesis

Dierk Raabe

d.raabe@mpi-susmat.de

Max-planck-institut Für Nachhaltige Materialien GmbH

Xinren Chen

Max-Planck-Institut for Sustainable Materials

Baptiste Bienvenu

Max-planck-institut Für Nachhaltige Materialien GmbH

Tingting Yang

Ernst Ruska-Centre for Microscopy and Spectroscopy with Electrons and Peter Grünberg Institute, Forschungszentrum Jülich, 52425 Jülich, Germany

Baptiste Gault

Max-planck-institut Für Nachhaltige Materialien GmbH

Shaolou Wei

Max-planck-institut Für Nachhaltige Materialien GmbH

Xuyang Zhou

Max-planck-institut Für Nachhaltige Materialien GmbH

Article

Keywords:

Posted Date: November 11th, 2025

DOI: https://doi.org/10.21203/rs.3.rs-7986257/v1

License: This work is licensed under a Creative Commons Attribution 4.0 International License.
Read Full License

Additional Declarations: There is **NO** Competing Interest.

Version of Record: A version of this preprint was published at Nature Synthesis on June 8th, 2026. See the published version at https://doi.org/10.1038/s44160-026-01086-5.

Solid–Solid Catalysis in Sustainable Alloy Synthesis

Xinren Chen[1], Baptiste Bienvenu[1], Tingting Yang[2], Baptiste Gault[1,3],

Shaolou Wei[1,*], Xuyang Zhou[1,4,*] and Dierk Raabe[1,*]

[1]Max Planck Institute for Sustainable Materials, 40237 Düsseldorf, Germany

[2]Ernst Ruska-Centre for Microscopy and Spectroscopy with Electrons and Peter Grünberg Institute, Forschungszentrum Jülich, 52425 Jülich, Germany

[3]Univ Rouen Normandie, CNRS, INSA Rouen Normandie, Groupe de Physique des Matériaux UMR 6634, F-76000 Rouen, France

[4]State Key Laboratory for Mechanical Behavior of Materials, Xi'an Jiaotong University, Center for Advancing Materials Performance from the Nanoscale (CAMP-Nano), 710049 Xi'an, P.R. China

Abstract

Metal production causes 10% of global greenhouse gas emissions, with most metals extracted from oxide ores via fossil-based pyrometallurgy including melting. Solid-state hydrogen-driven redox reduction is not only a sustainable alternative, but can also be used to integrate reduction, in-situ alloying of mixed oxides, and microstructure design in one step. Upon co-reduction of a Fe_2O_3–NiO mixture with hydrogen, we find a new type of solid–solid catalytic interaction between pre-reduced metal (Ni) and a transient oxide (FeO). This interaction accelerates hydrogen-based reduction by a factor of two—a remarkable effect given the scale of global metal production at nearly 2 billion tons annually. Specifically, during hydrogen-driven co-reduction of Fe_2O_3 and NiO, metal partitioning takes place across the metal-oxide interfaces, driven by interface dynamics during which restructuring continuously regenerates catalytic sites that promote H_2 spillover. These findings show that hydrogen-based alloy production is not only more sustainable than fossil-based practices but can leverage kinetic and commercial advantages through solid-solid catalytic effects.

Introduction

Metals are extracted from minerals, industrial waste and oxidized scrap through three main reduction principles[1]: pyrometallurgy, hydrometallurgy, and electrometallurgy. Pyrometallurgy

uses high homologous temperatures to smelt-reduce oxidic feedstock, such as Fe_2O_3 with CO in blast furnaces, a process globally responsible for ~10% energy use and ~8% CO_2 emissions, only considering steel production [2]. Hydrometallurgy uses aqueous leaching, purification, and recovery at lower temperatures [3], while electrometallurgy cathodically reduces metal ions from molten or aqueous ionic phases, as in Al extraction by the Hall–Héroult process, or purification through electrorefining.

For millennia, metal extraction technologies followed economic, scaling, and efficiency needs alone. Today, environmental and regulatory constraints challenge these traditional metal production routes, particularly in steelmaking [4], thereby motivating energy-efficient catalytic pathways[5] that are commercially viable. Solid-state direct reduction [6-9] offers such an alternative: it operates at moderate homologous temperatures, is solvent-free, scalable to million tons-per year reactors, and is accessible to various gaseous reductant types including sustainably produced hydrogen. Reduction kinetics is governed by redox conditions (temperature, pressure, reductants); transport mechanisms (reductants, redox product(s), metal, oxygen); catalysis effects; phase nucleation, growth and transformations; microstructure and damage; and micromechanical stress and strain fields [10]. Taking for instance Fe oxide as a model system, the CO or H_2 – based reduction of hematite (Fe_2O_3) to magnetite (Fe_3O_4) [11-13] follows Avrami nucleation and growth kinetics [14]. The subsequent magnetite-wüstite ($Fe_{1-x}O$, where x is the Fe deficiency) transformation is partly topotactic. This means both phases share an O^{2-} face-centered cubic (FCC) lattice, but it also involves cation rearrangement and non-ideal stoichiometry. $Fe_{1-x}O$ reduction proceeds via nucleation and growth or disproportionation ($Fe_{1-x}O \rightarrow Fe_3O_4 + Fe$), with associated volume changes and stresses complicating the final $Fe_{1-x}O \rightarrow Fe$ step [10,15]. The final transition to BCC Fe is diffusion-controlled [14], and the combined effects of mass loss, volumetric shrinkage, phase changes, and charge redistribution [16,17] qualify solid-state reduction as a highly complex open-system mechano-chemical process. In view of 2 billion tons of metals produced annually, understanding these mechanisms and their interplay is essential, for developing workflows and reactors to transform 6 millennia old practices into a more sustainable and cost-efficient industry.

Here, we report a newly discovered phenomenon in that context, namely, a solid-solid catalytic mechanism that supports metal extraction from oxide. It works by adding to a gas-solid reduction process of a transition metal oxide (here Fe_2O_3) a second catalytically acting metal (here Ni) or its reducible transition metal oxide precursor (here NiO), which can leverage several mechanisms that accelerate metal oxide reduction as evidenced in the following.

Solid–Solid catalysis

Conventional catalyst selection for hydrogen-based solid-gas direct reduction processes is guided by a volcano diagram of the hydrogen adsorption energies [18-20] (Fig. 1a). Per the Sabatier principle [21], activity peaks at intermediate binding strength. This sort of mechanistic screening highlights Ni, Co, W, and Cu as promising catalyst candidates for hydrogen-based Fe_2O_3 reduction, while noble metals, though active, are less economical. Among these, Ni [16,22,23] is especially attractive, as it also serves as alloying element in steels.

As shown in Fig. 1b, the addition of metallic Ni (particle size ~300 nm) noticeably shortens the Fe_2O_3 reduction saturation time at 700ºC by a factor of 1.6. However, the use of pure metallic catalysts necessitates carbon-intensive processes for metal extraction [9], thereby increasing both environmental and financial costs. To overcome this, we propose a co-reduction strategy that directly employs metal oxides or refined ores. Using bunsenite (NiO) (particle size ~15 μm) as an example, the co-reduction of the two oxides exhibits an even more pronounced catalytic effect, reducing the time-to-saturation state by a factor of 2 at 700 °C. As seen from the inset in Fig. 1b, the reaction rate remains consistently higher with NiO added rather than with metallic Ni addition or pure Fe_2O_3 alone. To deconvolute the apparent Fe_2O_3 conversion rate contribution due to NiO reduction, we provide the kinetic quantification after subtracting the NiO effect in fig. S1. Furthermore, the addition of Ni or NiO lowers the onset temperature of Fe_2O_3 reduction by at least ~100°C (fig. S2) when the process operates in a continuous heating manner, like under industrial direct reduction conditions. Such a catalytic process offers great potential to reduce both the temperature and time of Fe_2O_3 reduction while decreasing energy consumption, thereby enabling sustainable one-step production of Fe master alloys (Fig. 1c).

We attribute the catalytic effect at this reduction temperature to the H_2 spillover mechanism at metal–oxide interfaces [24-27]. As illustrated in Fig. 1d, NiO is rapidly reduced by H_2 [28], generating Ni–Fe oxide interfaces where the reduced Ni catalyzes H_2 dissociation and spillover [26,29-32], thereby accelerating the subsequent reduction of Fe oxides.

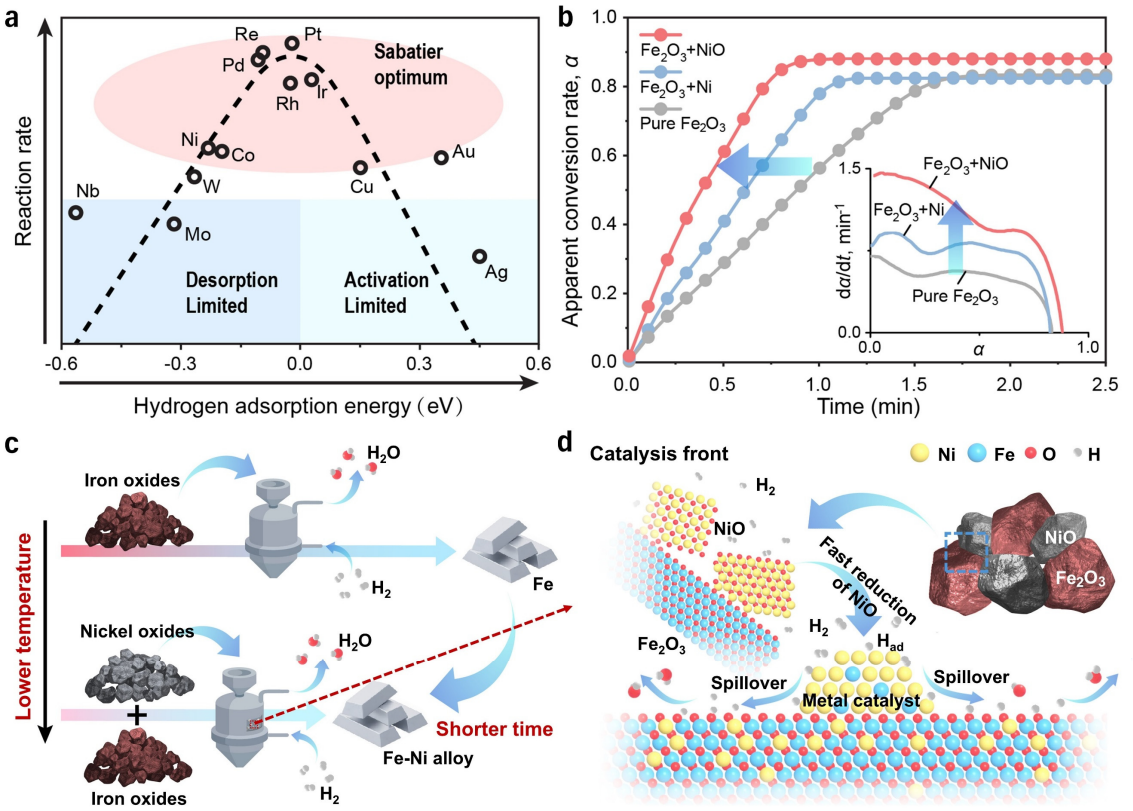

Figure 1. Catalyzing hydrogen-based iron-oxide reduction via Sabatier-optimized co-reduction. (**a**) Volcano plot of relative reaction rate versus H adsorption energy, compiled from the literature [20]. (**b**) Isothermal reduction of Fe_2O_3, Fe_2O_3 + Ni (Fe-36Ni wt.%) and Fe_2O_3 + NiO (Fe-36Ni wt.%) mixed powders at 700°C under a 10 L/h H_2 flow rate. The inset shows the first-order derivative ($d\alpha/dt$) as a function of conversion, indicating the change in reaction rate. (**c**) Schematic comparison of two different direct reduction pathways: upper row: non catalyzed version in which H_2 reduction separately produces Fe (from Fe_2O_3) before subsequently alloy production can be done. Bottom row: the same process, but with co-reducing a stoichiometric Fe_2O_3-NiO mixture, which forms a catalytic metal-oxide front and yields a Fe–Ni alloy in a shorter time. (**d**) Interfacial mechanism: reduced Ni (from NiO) creates an H_2-spillover front that accelerates Fe_2O_3 reduction and enables rapid alloy formation.

Kinetic enhancement mechanisms

We conducted an *in situ* synchrotron X-ray diffraction (SXRD) experiment to study the kinetics of hydrogen-based co-reduction of an Fe–Ni oxide model system with a moderate hydrogen flow rate of around 0.6 L/h to slow down the reduction process. Fig. 2a-c show that the main reaction cascade starts at 700°C (0 s), a stage in which the system contains Fe_3O_4 (converted from Fe_2O_3 during heating), NiO, and some metallic FCC Ni formed from partial reduction of NiO during heating. After 330 s at 700°C, NiO has been fully converted to metallic FCC Ni —

this initial step is considered as the "fast stage" of the reduction process [16]. Beyond this point, the main rate-limiting step commences, in which $Fe_{1-x}O$ gradually starts converting into metallic Fe. The *in situ* SXRD data focus on the kinetics and structural evolution during this slow, diffusion-controlled reduction stage. In hydrogen-based reduction, the transformations $Fe_2O_3 \rightarrow Fe_3O_4$ and $Fe_3O_4 \rightarrow Fe_{1-x}O$ proceed rapidly [6]. The rate-limiting step is $Fe_{1-x}O \rightarrow$ BCC Fe, which is hindered by slow hydrogen diffusion, incomplete H_2O removal [33,34] and a high nucleation barrier of BCC Fe [8,15,35-37].

From 0 s to 1230 s under isothermal conditions (700°C), the SXRD data show progressive intensity changes of the Fe_3O_4 and $Fe_{1-x}O$ peaks (Fig. 2a). During the reduction, no BCC phase emerged (Fig. 2b). Instead, a lattice-parameter shift in the metallic FCC Ni phase (Fig. 2c) indicates the partitioning and diffusion of Fe atoms into the Ni lattice. After 1230 s, most of the reduction and alloying processes were complete. SXRD patterns of bulk samples further holding at 700°C for 1 h (Fig. 2d) confirm that, in the presence of NiO, FCC phase is formed without BCC phase (which remains the only product in the case of pure Fe_2O_3 reduction). Compared with the interdiffusion reference (pressed bulk of Fe ~400 nm and Ni ~300 nm powders), which shows clear BCC peaks after the same heat treatment, the Fe_2O_3 + NiO system exhibits a markedly accelerated alloying process during the reduction.

At 730 s, high-angle annular dark-field scanning transmission electron microscopy (HAADF-STEM) imaging reveals the interface between the FCC (Fe, Ni) phase and residual $Fe_{1-x}O$ (Fig. 2e and fig. S3). The corresponding energy-dispersive X-ray spectroscopy (EDS) elemental maps of Fe, Ni, and O (Fig. 2f–h) show Fe enrichment at the interface between the FCC Fe–Ni phase and $Fe_{1-x}O$, as well as along the grain boundary between two FCC grains. By phase indexing of four-dimensional scanning transmission electron microscopy (4D-STEM) data, no additional FCC phase formation was detected during this period (fig. S4). At 1230 s, the EDS map (fig. S5) shows a uniform Fe–Ni distribution with no detectable oxides and confirms that the initially Ni-rich phase has transformed into the designed Fe–Ni alloy.

This accelerated process is illustrated in Fig. 2i, where the mixture of the FCC Ni-rich phase and $Fe_{1-x}O$ directly reduces to an FCC Fe–Ni alloy without formation of any intermediate BCC Fe phase. This means that the first formed Ni metal acts as a direct metallothermic reductant extracting Fe out of its oxide state. Notably, when compared to the conventional interdiffusion process between Fe and Ni, as shown in Fig. 2j and k, alloy formation is significantly accelerated. Based on the thermophysical data from the TCFE9 and MOBFE4 databases

(Thermo-Calc Software), tracer diffusivity calculations suggest that, under equilibrium conditions at 700°C for 1200 s, Fe and Ni should each diffuse only ~10 nm in the Fe–Ni alloy (Fig. 2i), a value far below the critical length scale necessary for the formation of a homogenous Fe-Ni alloy. Interdiffusion simulations further confirm that achieving complete homogenization in a system of comparable dimensions would typically require over 5 days (120 hours) at such a low temperature (Fig. 2j). In contrast, the *in situ* SXRD results reveal that alloying in our new reaction pathway is completed within only 30 minutes, implying that the presence of NiO precursors significantly enhance Fe–Ni interdiffusion and alloy homogenization beyond predictions from conventional bulk diffusion models.

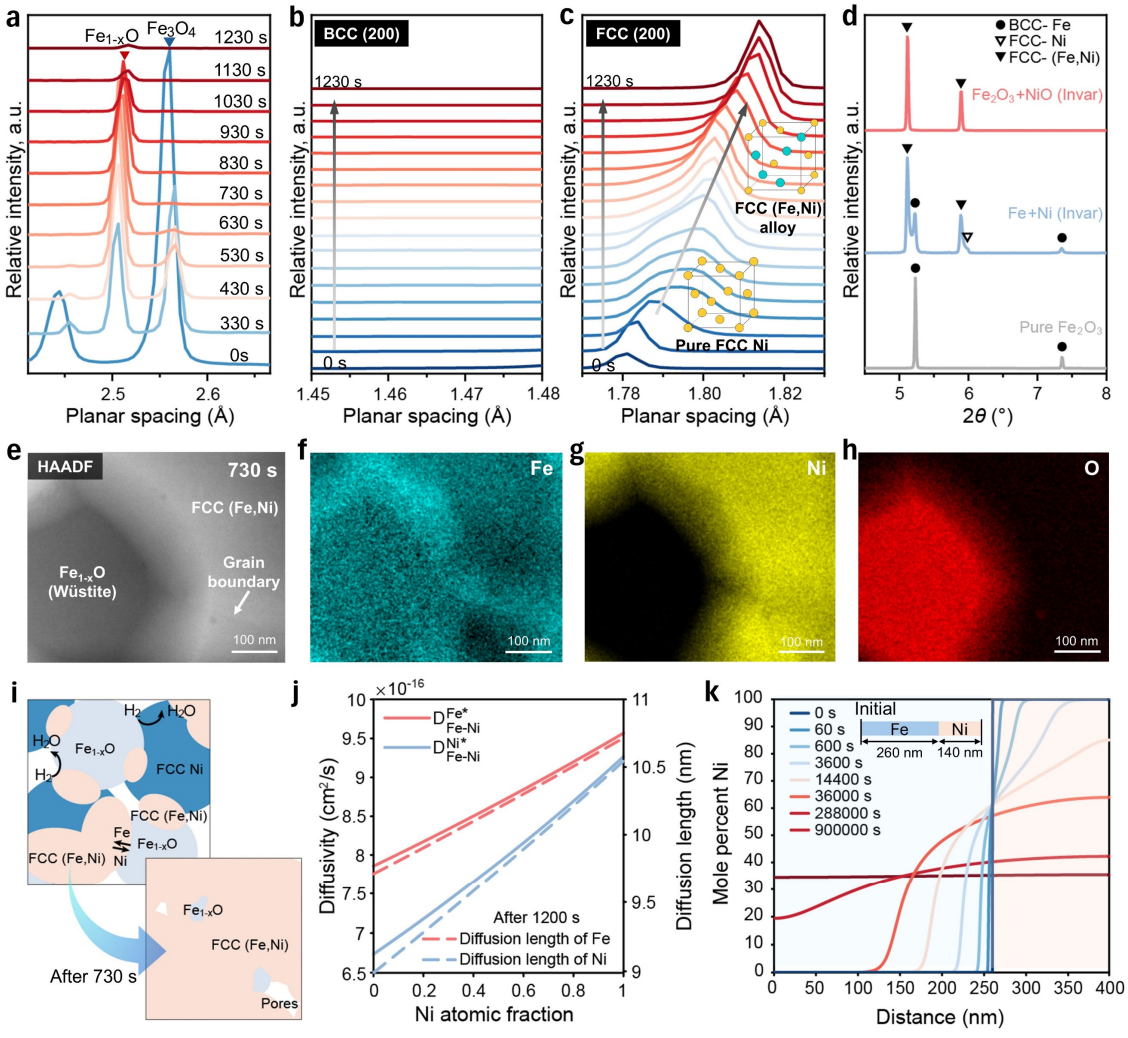

Figure 2. Time-resolved characterization of the hydrogen-based reduction and alloying. (**a**) *In situ* synchrotron X-ray diffraction (SXRD) patterns during hydrogen reduction of Fe_2O_3 + NiO (Fe–36Ni wt.%) at 700°C at a ~0.6 L/h H_2 flow rate, showing a full conversion of Fe_2O_3 to Fe_3O_4 after reaching 700 °C, followed by the fast disappearance of Fe_3O_4 phase and the persistence and gradual reduction of $Fe_{1-x}O$. Data reproduced from Ref. [16]. (**b**) Zoomed-in SXRD patterns showing no emergence of the BCC metal (200) peak. (**c**) Zoomed-in SXRD patterns showing the evolution of the FCC metal (200) peak. (**d**) SXRD patterns of the reduction of bulk samples after holding at 700°C for 1 h comparing pure Fe_2O_3, Fe_2O_3 + NiO (Fe–36Ni wt.%), and an interdiffusion reference of Fe + Ni (Fe–36Ni wt.%). (**e**) High-angle annular dark-field scanning transmission electron microscopy (HAADF-STEM) image at 730 s. (**f–h**) Corresponding energy-dispersive X-ray spectroscopy (EDS) maps of Fe, Ni, and O. (**i**) Schematic of the reaction pathway showing the interface evolution between $Fe_{1-x}O$ and the earlier-reduced Ni at 730 s during hydrogen-based reduction. (**j**) Calculated tracer diffusivities of Fe and Ni in FCC Fe-36Ni wt.% alloy at 700°C as functions of Ni content (left axis), with corresponding diffusion lengths after 1200 s (right axis). (**k**) Simulated interdiffusion profiles of Ni concentration across a Fe/Ni interface at different times, based on thermodynamic and mobility databases (TCFE9 and MOBFE4), showing gradual alloying toward the final Fe–Ni invar composition.

Structure and chemistry of the metal/oxide interfaces

To more precisely characterize the chemical composition near the metal-oxide interfaces and thus elucidate the reaction mechanism at the interface between metallic FCC grains and $Fe_{1-x}O$, an atom probe tomography (APT) specimen containing such interfaces was prepared, as illustrated in Fig. 3a. The $Fe_{1-x}O$ phase is identified by 4D-STEM performed on the APT specimen, as highlighted through virtual dark-field imaging (inset in Fig. 3a) of the corresponding diffraction spots (Fig. S6). The accompanying orientation map reveals the presence of five distinct metallic FCC grains (denoted as γ1 to γ5 on Fig. 3b) and the oxidic $Fe_{1-x}O$ phase, each with different crystallographic orientations. This configuration allows for the analysis of multiple $Fe_{1-x}O$-FCC interfaces within a single sample. Due to the spatial overlap between the $Fe_{1-x}O$ and FCC phases, virtual dark-field images were employed to enhance the contrast and clearly delineate their morphology and distribution, as presented in Fig. 3b and fig. S6.

For studying the same region at highest chemical sensitivity, correlative APT results are presented in Fig. 3c, where iso-surfaces in the concentration of Ni (37 at.%), Fe (58 at.%), and O (30 at.%) delineate the grain structures, enabling direct spatial comparison with the 4D-STEM data in Fig. 3b. To investigate elemental distributions at the reduction and alloying fronts, two distinct locations were analyzed: one at the interface between the sintering neck (site 1) and $Fe_{1-x}O$, and another at the boundary between a metallic FCC grain (γ3) and $Fe_{1-x}O$ (site 2). At site 1, as shown in Fig. 3d, an Fe-enriched region appears on the metal side adjacent to the metal–oxide interface. This observation suggests that Ni atoms diffusing from the surfaces of Ni precursor grains combine with the reduced Fe, promoting growth of a metallic FCC (Fe, Ni) phase, instead of forming BCC Fe. In contrast, at the FCC-γ3/$Fe_{1-x}O$ interface (site 2), partitioning between Fe and Ni is observed (Fig. 3e). Interestingly, a ~7 at.% Ni enrichment is detected on the $Fe_{1-x}O$ side of the interface (Fig. 3f). This observation suggests that Ni also partitions directly into the metal-oxide interface, a phenomenon not previously reported.

Figure 3g illustrates two reaction-driven alloying mechanisms that are likely responsible for the formation of the FCC (Fe, Ni) phase. In Mechanism 1 (site 1), Ni and Fe from adjacent FCC grains (*e.g.* γ2 and γ3) migrate via surface and grain boundary diffusion, forming a localized “sintering neck”, and the outward migration and reduction of Fe^{2+} ions from $Fe_{1-x}O$ and inward diffusion of Ni result in the formation of an Fe-enriched metallic FCC alloy at the neck interface. This process is driven by redox reactions and the minimization of surface energy.

In Mechanism 2 (site 2), Ni diffuses directly along the $Fe_{1-x}O$ interface into regions where Fe is being reduced by hydrogen, enabling the growth of a continuous FCC (Fe, Ni) phase (fig. S7) without a sintering neck. Although there is a difference in diffusion micro-mechanisms, both phenomena emphasize the coupling of elemental diffusion with hydrogen-induced reduction to produce the observed transformations and solid solution states.

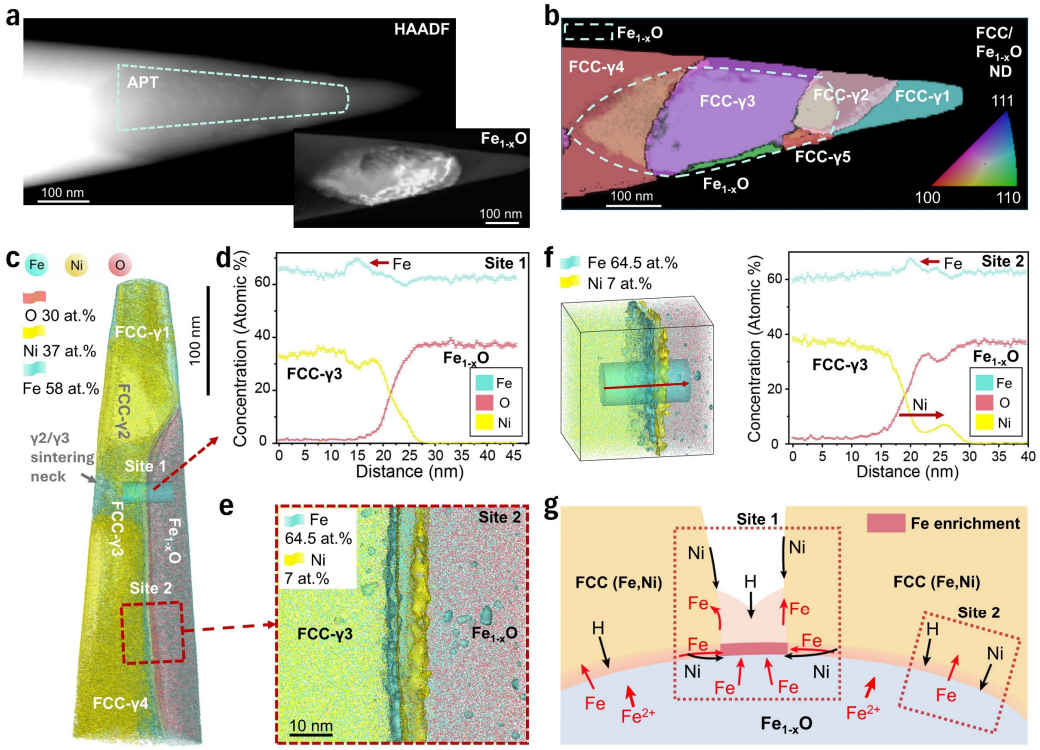

Figure 3. Nanoscale reaction interfaces during hydrogen-based reduction. (**a**) HAADF-STEM image of a needle-shaped atom probe tomography (APT) specimen extracted from the reaction interface between FCC (Fe, Ni) grains and $Fe_{1-x}O$. The inset is the four-dimensional scanning transmission electron microscopy (4D-STEM) virtual dark-field image of embedded $Fe_{1-x}O$ (fig. S6). (**b**) Correlative 4D-STEM grain orientation map of the same specimen, showing five FCC grains (γ1–γ5) adjacent to $Fe_{1-x}O$, indexed along the normal direction (ND). (**c**) APT 3D reconstruction showing spatial distributions of Fe, Ni, and O across FCC grains (γ2–γ4) and neighboring $Fe_{1-x}O$ regions. (**d**) One-dimensional (1D) atomic concentration profile across the FCC–$Fe_{1-x}O$ interface (site 1) at the sintering neck. (**e-f**) Local composition maps at site 2 and 1D profiles across the FCC γ3/$Fe_{1-x}O$ interface. (**g**) Schematic of two proposed reduction mechanisms occurring at sites 1 and 2, respectively.

Spillover-driven local interfacial redox partitioning cycle

Metal-oxide interfaces play a critical role in redox catalysis [38-40], where oxygen vacancies facilitate charge transfer dynamics [41]. Incorporation of Ni enhances H_2 dissociation and spillover [26,29,30], sustaining catalytic activity.

During hydrogen reduction of $Fe_{1-x}O$ (Fig. 4a and b), Ni effectively splits the H_2 into adsorbed H atoms on metal surface or interfaces [42], which migrate to the adjacent oxide (H_2 spillover) and facilitating oxygen removal [43]. Lattice oxygen (O^{2-}) reacts with spillover H to form H_2O, creating oxygen vacancies ($V_O^{\cdot\cdot}$, Kröger-Vink notation [44]) Charge neutrality is maintained by creating cation vacancies (V_{Fe}'') [45]. These vacancies distort local coordination, attracting nearby Fe into tetrahedral sites that temporarily impede reduction. As H_2 is consumed and P_{H_2O} rises, both Fe and Ni are reoxidized [33] (Fig. 4c). Ni^{2+} perturbs the lattice, destabilizing Fe in tetrahedral sites [46] and enabling renewed reduction (Fig. 4d). In the next step, Ni^{2+} is reduced back to Ni, regenerating active Ni–$Fe_{1-x}O$ interfaces. Repeated cycles leave a transient Ni-enriched layer in $Fe_{1-x}O$ (Fig. 3e), coupling rapid H_2 activation on Ni with fast co-reduction of Ni and Fe to drive FCC alloy growth [31], bypassing the usually expected conventional BCC nucleation pathway.

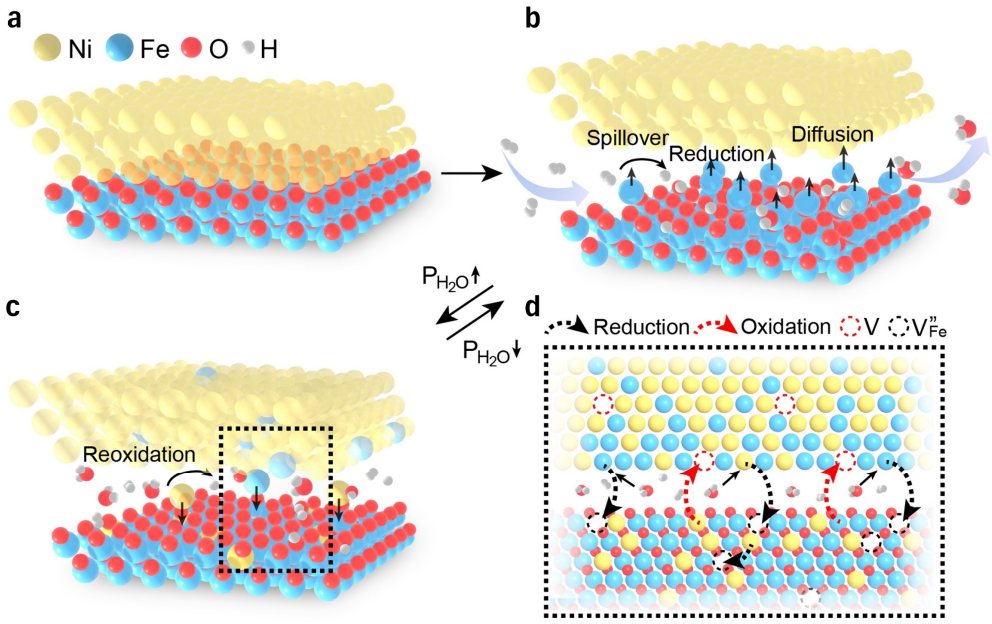

Figure 4: **Schematic of the hydrogen spillover–driven redox cycle at the metal-oxide interface:** (**a**) Early-reduced Ni contact $Fe_{1-x}O$. (**b**) H_2 molecules dissociate on Ni and spill over to $Fe_{1-x}O$, promoting interfacial reduction. (**c**) The interfacial region undergoes reoxidation. (**d**) Zoom-in of the front: coupled reduction/oxidation

loops generate/annihilate point defects (e.g. V: vacancy in the FCC lattice, V''_{Fe}: cation vacancy), continually regenerating active sites and sustaining accelerated $Fe_{1-x}O$ reduction and alloying with Ni.

Figure 4 sketches how the reaction front evolves dynamically. The formation of Ni^{2+} inclusions during reoxidation, with Fe^{2+} being reduced, is a redox-related partitioning step within $Fe_{1-x}O$ that may be driven by thermodynamic partitioning at the metal–oxide interface. To quantify this effect, we performed DFT calculations (see Methods) and defined the partitioning enthalpy H_P as the energy difference between the pristine and the co-substituted systems, respectively (Fig. 5a). For bulk metallic FCC Ni and stoichiometric FeO, DFT calculations based on the metaGGA-r^{2}SCAN x-c functional predict H_P of -0.26 eV, indicating a strong thermodynamic driving force for solid-state partitioning and direct reduction of the oxide through metallic Ni. Supplementary Table S1 shows that the Ni–FeO pair exhibits the strongest driving force among all Ni/Fe–oxide combinations.

For this analysis, we consider a prototypical coherent interface model having a $\{111\}_{FCC}$ to $\{111\}_{FeO}$ orientation relationship, minimizing the lattice mismatch between the two materials to approximately 2%, depending on the x-c functional used in the DFT calculations. This interface has two different configurations, depending on whether a Fe or a O-terminated {111} layer of stoichiometric FeO is in contact with FCC Ni (see Fig. 5b). DFT simulations predict H_P = +0.25 eV for the Fe-terminated interface (partitioning unfavorable) and –0.21 eV for the O-terminated interface (partitioning favorable), consistent with bulk behavior. Thus, intermixing can proceed as the interface migrates during reduction, supporting our experimental observations of Ni^{2+} partitioning and enhanced reaction kinetics.

Across redox cycles, Fe and Ni re-enter $Fe_{1-x}O$ cation sites, generating vacancies at the FCC (Ni,Fe) surface. These vacancies may readily cluster into voids at 700°C but can also be refilled by reduced Fe in subsequent cycles, leveraging enhanced diffusion and promoting alloying. This mechanism likely accounts for the diffusion enhancement that underpins the accelerated alloying described above.

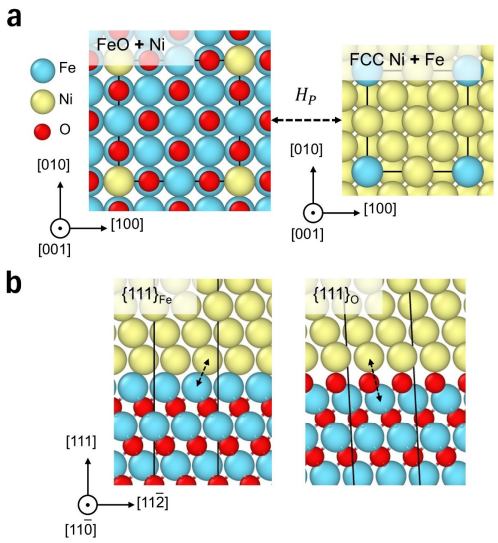

Figure 5: **Solid-state partitioning between metallic FCC Ni and stoichiometric FeO based on DFT calculations**. (**a**) Structural models used in the DFT calculations representing the bulk partitioning tendency between FCC Ni and stoichiometric FeO. (**b**) The two Fe and O-terminated configurations of the $\{111\}_{Ni}/\{111\}_{FeO}$ interface considered in the DFT calculations. The two dashed arrows indicate the Fe and Ni atoms that are swapped for evaluating the partitioning enthalpy H_P at the interface. Thick black lines show the limit of the periodic simulation cells used in the simulations.

We note that a simple thermodynamic descriptor as the value of H_P allows for a fast screening of promising oxide systems which are prone to exhibit such mechanism in the context of similar solid-state catalytic reaction pathways, potentially reducing the required hydrogen partial pressure and overall cost of such one-step metallurgical processes.

In summary, we demonstrate a twofold kinetic enhancement in the single-step hydrogen co-reduction of Fe_2O_3 with NiO, yielding Fe–Ni alloys via a previously unrecognized solid–solid catalytic pathway. Reduction of NiO produces Ni-rich FCC domains that: (I) catalyze $Fe_{1-x}O$ reduction through H_2 spillover at dynamically reorganizing metal–oxide interfaces; (II) undergo redox-driven partitioning into Fe oxides, regenerating active interfaces; and (III) directly alloy with reduced Fe at accelerated diffusional rates, bypassing the nucleation barrier of BCC Fe. These coupled effects enable rapid FCC Fe–Ni alloy formation at 700°C, cutting energy use and CO_2 emissions while reducing reliance on carbon-intensive routes. The findings constitute novel mechanistic insights that can leverage a big leap toward more sustainable metallurgical extraction methods.

Methods:

Material preparations

Fe_2O_3 and NiO powders (325 mesh, <44 μm, ≥99.7% purity) were selected as the starting materials, while Ni powders (200–300 nm, ≥99.9% purity) were employed for comparison. The powders were proportioned to match the Fe–Ni composition of the conventional Fe–36 wt.% Ni invar alloy (equivalent to Fe–34.8 at.% Ni) and thoroughly homogenized in an agate mortar and pestle. The mixed powders were used for kinetic studies of the catalytic effect. For bulk reduction experiments, the mixtures were pressed into cylindrical pellets (≈13 mm in diameter and 2 mm in thickness) using a hydraulic press at a load of ~3.75 tonnes. For subsequent 4D-STEM and APT analyses, site-specific specimens were prepared using a plasma-focused ion beam (PFIB, FEI Helios) equipped with an Xe-ion source. A final low-energy cleaning step (5 kV, 10 pA plasma beam) was applied to minimize ion implantation and surface amorphization due to its limited penetration depth.

Thermogravimetric analysis

Reduction behavior was studied using a custom thermal balance placed inside an infrared furnace. To examine the catalytic effect on reduction kinetics and to eliminate any sample size effects, mixed powders (50 mg) were first heated in argon (99.999% purity) at 20 °C/min to 700 °C, then exposed to hydrogen (10 L/h, 99.999% purity) under an isothermal condition for 30 min, followed by cooling to room temperature in argon. For bulk reduction, the powders were compacted into pellets with ~6.35 mm diameters at ~2 mm thickness. Continuous heating reduction experiments were conducted using these compacted pellets heated in hydrogen (10 L/h, 99.999% purity) at 5 °C min^{-1} to 700 °C, followed by an isothermal hold section in hydrogen (10 L/h, 99.999% purity) for 2 h before cooling. Instantaneous mass loss was continuously monitored, and conversion fractions were calculated by dividing the observed weight loss by the theoretical weight loss expected for complete $Fe_2O_3 \rightarrow Fe$ and $NiO \rightarrow Ni$ reduction. Intermediate states were obtained by quenching with high-flow Ar.

In situ SXRD study

In situ synchrotron X-ray experiments were performed at beamline P02.1 of PETRA III (DESY), utilizing a high-energy X-ray beam with a wavelength of 0.20735 Å. A working distance of 1,700 mm was selected to achieve an optimal compromise between angular resolution and the number of observable Debye–Scherrer rings; this was precisely calibrated using standard LaB_6 powders from NIST. For the measurements, the pre-compacted Fe_2O_3 and NiO powders were sealed inside a fused silica capillary tube (inner diameter ~0.6 mm), with a standard type-K thermocouple positioned adjacent to the sample for accurate temperature monitoring. Heating was achieved via a hot air blower integrated with a PID (proportional–integral–derivative) controller. Additional calibration was performed to correct for discrepancies between the set temperature of the blower and the actual sample temperature. High purity H_2 (purity 99.999%, 1 atom) was introduced through the capillary during heating at a moderate flow rate of ~0.6 L/h to reduce convection-induced cooling. Two-dimensional diffraction patterns were recorded every 2 seconds with a beam footprint of 500 × 500 μm² to capture the onset of reduction and phase evolution. Data processing was carried out using the open-source software GSAS-II [47]. Azimuthal integration was limited to one quadrant (0°–90°) of each Debye–Scherrer ring, and peak shifts were evaluated using a Gaussian–Lorentzian fitting algorithm [48]. Quantitative phase analysis was conducted through Rietveld refinement, ensuring that each fit achieved a weighted-profile *R*-factor (R_{wp}) below 10%.

4D-STEM characterization

We employed 4D-STEM to analyze the crystallographic orientations and phase distributions within the reaction products. The initial 4D-STEM measurements were conducted using a JEM-2200FS microscope (JEOL Ltd.) operated at an accelerating voltage of 200 kV. This instrument was equipped with a NanoMEGAS precession electron diffraction (PED) system, operated at a frequency of 100 Hz with a precession half-angle of 0.1°, allowing for enhanced orientation precision and reduction of dynamical diffraction effects.

Complementary 4D-STEM data were acquired using a Tescan TENSOR STEM instrument at the Ernst Ruska-Centre (ER-C), Forschungszentrum Jülich. This system was operated at 100 kV and used a higher precession angle of 0.5° to improve the reliability of phase and orientation mapping in fine-grained regions. A fast pixelated STEM detector enabled the collection of full diffraction patterns at each probe position across the scanned area.

The data were processed using the commercial ASTAR/ACOM software suite (NanoMEGAS), which performs template matching of experimental diffraction patterns against simulated patterns to generate orientation and phase maps. Virtual bright-field (VBF) and virtual dark-field (VDF) images were reconstructed from the 4D-STEM dataset to enhance contrast and facilitate interpretation. The resulting crystallographic maps revealed the spatial arrangement of FCC grains, residual $Fe_{1-x}O$ regions, GBs, and twin boundaries (TBs).

Correlative atom probe tomography

Following the acquisition of 4D-STEM data, we performed APT analysis on exactly the same needle-shaped specimen to enable fully correlative structural and compositional analysis at the atomic scale. The APT measurements were carried out using a LEAP 5000XR instrument (CAMECA Instruments), operated at a specimen temperature of 90 K. Laser pulsing conditions were set to a pulse energy of 100 pJ and a pulse rate of 200 kHz, with an average detection rate of 1%. Data processing and 3D reconstruction were performed using the AP Suite 6.3 software (CAMECA), with the image compression factor and *k*-factor determined through iterative alignment with the STEM image of the specimen to achieve accurate spatial fidelity. To quantify elemental distributions across interfaces, one-dimensional (1D) composition profiles were extracted using a cylindrical region of interest with a diameter of 20 nm and a sampling step of 0.5 nm.

Simulation details

Atomistic simulations are performed within Density Functional Theory (DFT), as implemented in the VASP code [49]. Projector-augmented wave pseudopotentials are used to model Fe, Ni and O atoms, containing 8, 10 and 6 valence electrons, respectively. The Brillouin zone was sampled using a grid with a smallest spacing of 0.15 $Å^{-1}$ between k points. For this analysis, we performed DFT calculations considering two different exchange and correlation (x-c) functionals, namely the GGA-PBE and the metaGGA-r^{2}SCAN. While GGA functionals underestimate thermodynamic properties of transition metal oxides, such as their formation enthalpies, the later metaGGA-r^{2}SCAN x-c functional yields a much better agreement with experimental references [50,51] while remaining a semi-local method, thus motivating for its use in the present analysis. For these reasons, we expect DFT results obtained with the metaGGA

x-c functional to be more robust and accurate for the rationalization of the thermodynamic driving force behind the observed solid-state partitioning and thus focus on these results for further analysis. Results according to both DFT x-c functionals are presented in details in Supplementary Tables 1 and 2. We used the two GGA-PBE and metaGGA-r^{2}SCAN [50] exchange and correlation functionals in all presented calculations.

All DFT calculations are spin-polarized in the collinear approximation, since all considered materials have an ordered magnetic ground state, namely ferromagnetic for both BCC Fe and FCC Ni, antiferromagnetic along <111> directions for FeO and NiO, ferrimagnetic for Fe_3O_4, and antiferromagnetic along the [0001] direction for Fe_2O_3.

All bulk prototypes are fully relaxed until all components of the remaining forces acting on atoms and stresses on the simulation cells fall below 5 meV.Å^{-1} and 5 meV.Å^{-2}, respectively. The bulk partitioning enthalpy H_P between two materials containing A and B metal species, respectively, is defined as:

$$H_P = [E(A^{+B}) + E(B^{+A})] - [E(A) + E(B)],$$

where $E(A^{+B})$ and $E(B^{+A})$ are the DFT total energies of a simulation cell containing bulk A with one substitutional B atom, and bulk B with one A atom, respectively, while $E(A)$ and $E(B)$ are the total energies of the two pristine bulk materials.

The structural models used to model the two configurations of the FCC Ni/FeO interface, the $\{111\}_{Fe}$ and $\{111\}_{O}$-terminated structures presented in Fig. 5b, respectively contain 7 layers of Ni and 9 layers of FeO, and 8 layers of Ni and 11 layers of FeO in the [111] directions. Both the FCC Ni and FeO slabs are equally strained to accommodate the lattice mismatch between the two materials. The equilibrium position of the two FCC Ni and FeO slabs with respect to each other is then determined, before the interface is fully relaxed with respect to the direction perpendicular to the interface plane and the positions of the atoms. The partitioning enthalpy at the interface is then evaluated by swapping one Ni atom of the FCC slab with one Fe atom from the FeO slab, both coming from the closest atomic plane to the interface.

Acknowledgments

SXRD measurements were carried out at beamlines P02.1 and P21.1, PETRA III of Deutsches Elektronen-Synchrotron (DESY, proposal Nos. I-20231121, I-20240759, I-20240761, and I-

20240761). We thank Uwe Tezins and Andreas Sturm for their support to the FIB & APT facilities at MPI Sus-mat. **Funding:** X.C. and B.G. gratefully acknowledge the Collaborative Research Centre/Transregio (CRC/TRR) 270 HoMMage-Z01 project funded by the Deutsche Forschungsgemeinschaft (DFG). S.L.W. acknowledges financial support from Alexander von Humboldt Research Fellowship (hosted by D.R.). D.R. is grateful for the financial support through the ERC Advanced Grant ROC (grant agreement No 101054368). X.Z. acknowledges support from National Natural Science Fund for Excellent Young Scientists Fund Program (Overseas). **Author contributions:** S.L.W., X.Z., and D.R. conceived the idea and supervised the project. X.C., S.L.W. and T.Y. performed the experiments and analyzed the data. B.G. assisted with the atom probe data analysis. X.Z. assisted with the electron microscopy data analysis. B.B. performed the atomistic simulations. X.C., S.L.W., X.Z., and D.R. rationalized all the results. X.C., B.B., and D.R. wrote the original draft of the manuscript. D.R. acquired the funding for this research. All authors discussed and approved the final version of the manuscript. **Competing interests:** The authors declare no competing interests. **Data and materials availability:** All data needed to evaluate the conclusions in the paper are present in the paper and/or the Supplementary Materials. Additional data related to this paper may be requested from the authors.

References

1 Hiorns, A. H. *Principles of metallurgy*. (Macmillan and Company, 1914).

2 Raabe, D., Tasan, C. C. & Olivetti, E. A. Strategies for improving the sustainability of structural metals. *Nature* **575**, 64-74 (2019).

3 Harvey, J.-P. *et al.* Greener reactants, renewable energies and environmental impact mitigation strategies in pyrometallurgical processes: A review. *MRS Energy Sustain.* **9**, 212-247 (2022).

4 Watari, T., Hata, S., Nakajima, K. & Nansai, K. Limited quantity and quality of steel supply in a zero-emission future. *Nat. Sustain.* **6**, 336-343 (2023).

5 van Deelen, T. W., Hernández Mejía, C. & de Jong, K. P. Control of metal-support interactions in heterogeneous catalysts to enhance activity and selectivity. *Nat. Catal.* **2**, 955-970 (2019).

6 Turkdogan, E. & Vinters, J. Gaseous reduction of iron oxides: Part I. Reduction of hematite in hydrogen. *Metall. Mater. Trans. B* **2**, 3175-3188 (1971).

7 Wang, R. R., Zhao, Y. Q., Babich, A., Senk, D. & Fan, X. Y. Hydrogen direct reduction (H-DR) in steel industry—An overview of challenges and opportunities. *J. Clean. Prod.* **329**, 129797 (2021).

8 Spreitzer, D. & Schenk, J. Reduction of iron oxides with hydrogen—A review. *Steel Res. Int.* **90**, 1900108 (2019).

9 Raabe, D. The materials science behind sustainable metals and alloys. *Chem. Rev.* **123**, 2436-2608 (2023).

10 Meyers, M. A. & Tantevee, T. Stresses induced in iron-ore pellets by hydrogen reduction. *Metall. Trans. B* **17**, 217-227 (1986).

11 Turkdogan, E. T., Olsson, R. G. & Vinters, J. V. Gaseous reduction of iron oxides: Part II. Pore characteristics of iron reduced from hematite in hydrogen. *Metall. Trans.* **2**, 3189-3196 (1971).

12 El-Geassy, A. A. & Nasr, M. I. Influence of the original structure on the kinetics of hydrogen reduction of hematite compacts. *Trans. Iron Steel Inst. Jpn.* **28**, 650-658 (1988).

13 Cavaliere, P., Perrone, A., Marsano, D. & Primavera, V. Hydrogen‐based direct reduction of iron oxides pellets modeling. *Steel Res. Int.* **94**, 2200791 (2023).

14 Avrami, M. Kinetics of phase change. I General theory. *J. Chem. Phys.* **7**, 1103-1112 (1939).

15 Bai, Y. *et al.* Chemo-mechanical phase-field modeling of iron oxide reduction with hydrogen. *Acta Mater.* **231**, 117899 (2022).

16 Wei, S., Ma, Y. & Raabe, D. One step from oxides to sustainable bulk alloys. *Nature*, 1-7 (2024).

17 Zhou, X. *et al.* Complexions at the iron-magnetite interface. *Nat. Commun.* **16**, 2705 (2025).

18 Pozzo, M. & Alfe, D. Hydrogen dissociation and diffusion on transition metal (= Ti, Zr, V, Fe, Ru, Co, Rh, Ni, Pd, Cu, Ag)-doped Mg (0001) surfaces. *Int. J. Hydrogen Energy* **34**, 1922-1930 (2009).

19 Conway, B. & Bockris, J. O. M. The *d*-band character of metals and the rate and mechanism of the electrolytic hydrogen evolution reaction. *Nature* **178**, 488-489 (1956).

20 Nørskov, J. K. *et al.* Trends in the exchange current for hydrogen evolution. *J. Electrochem. Soc.* **152**, J23 (2005).

21 Hu, S. & Li, W.-X. Sabatier principle of metal-support interaction for design of ultrastable metal nanocatalysts. *Science* **374**, 1360-1365 (2021).

22 Minaev, E. & Mryakina, T. Alloyed powders produced by reduction of a complex oxide. *Sov. Powder Metall. Met. Ceram.* **7**, 83-85 (1968).

23 de Alvarenga Oliveira, V., de Jesus Taveira Lana, R., da Silva Coelho, H. C., Brigolini, G. J. S. & dos Santos, C. G. Kinetic studies of the reduction of limonitic nickel ore by hydrogen. *Metall. Mater. Trans. B* **51**, 1418-1431 (2020).

24 Liu, X., Fu, Q. & Shen, X. Theoretical study of hydrogen desorption on the Ni (100) surface through simulated temperature programmed desorption spectra. *Surf. Sci.* **744**, 122467 (2024).

25 van Helden, P., van den Berg, J.-A. & Weststrate, C. J. Hydrogen adsorption on Co surfaces: a density functional theory and temperature programmed desorption study. *ACS Catal.* **2**, 1097-1107 (2012).

26 Sermon, P. & Bond, G. Hydrogen spillover. *Catal. Rev.* **8**, 211-239 (1974).

27 Wang, T. *et al.* Nature of metal-support interaction for metal catalysts on oxide supports. *Science* **386**, 915-920 (2024).

28 Parravano, G. The reduction of nickel oxide by hydrogen. *J. Am. Chem. Soc.* **74**, 1194-1198 (1952).

29 Zaera, F. The long and winding road to catalysis. *Nature* **541**, 37-38 (2017).

30 Shen, H., Li, H., Yang, Z. & Li, C. Magic of hydrogen spillover: Understanding and application. *Green Energy & Environment* **7**, 1161-1198 (2022).

31 Pan, Y. *et al.* Alloying effects on iron oxide redox pathways: Insights into sustainable hydrogen-based reduction. *J. Phys. Chem. Lett.*, 5506-5514 (2025).

32 Sastri, M. V. C., Viswanath, R. P. & Viswanathan, B. Studies on the reduction of iron oxide with hydrogen. *Int. J. Hydrogen Energy* **7**, 951-955 (1982).

33 Zhou, X. *et al.* Effect of pore formation on redox-driven phase transformation. *Phys. Rev. Lett.* **130**, 168001 (2023).
34 He, K., Zheng, Z. & Chen, Z. A numerical investigation on the hydrogen reduction of wüstite using a 2D mesoscale method. *Int. J. Hydrogen Energy* **47**, 8118-8129 (2022).
35 Moujahid, S. E. & Rist, A. The nucleation of iron on dense wustite: A morphological study. *Metall. Trans. B* **19**, 787-802 (1988).
36 Kim, S.-H. *et al.* Influence of microstructure and atomic-scale chemistry on the direct reduction of iron ore with hydrogen at 700°C. *Acta Mater.* **212**, 116933 (2021).
37 Meng, Q., Rong, Y. & Hsu, T. Y. Nucleation barrier for phase transformations in nanosized crystals. *Phys. Rev. B* **65**, 174118 (2002).
38 Chen, M. S. & Goodman, D. W. The structure of catalytically active gold on titania. *Science* **306**, 252-255 (2004).
39 Tang, H. *et al.* Classical strong metal–support interactions between gold nanoparticles and titanium dioxide. *Sci. Adv.* **3**, e1700231 (2017).
40 Cargnello, M. *et al.* Control of metal nanocrystal size reveals metal-support interface role for ceria catalysts. *Science* **341**, 771-773 (2013).
41 Rousseau, R., Glezakou, V.-A. & Selloni, A. Theoretical insights into the surface physics and chemistry of redox-active oxides. *Nat. Rev. Mater.* **5**, 460-475 (2020).
42 Somorjai, G. A. & Li, Y. *Introduction to surface chemistry and catalysis*. Vol. 2 (Wiley New York, 1994).
43 Ruiz Puigdollers, A., Schlexer, P., Tosoni, S. & Pacchioni, G. Increasing oxide reducibility: the role of metal/oxide interfaces in the formation of oxygen vacancies. *ACS Catal.* **7**, 6493-6513 (2017).
44 Kröger, F. & Vink, H. Solid State Physics. *Academic Press, New York* **3**, 307 (1956).
45 Radler, M. J., Cohen, J. B. & Faber, J. Point defect clusters in wüstite. *J. Phys. Chem. Solids* **51**, 217-228 (1990).
46 Liang, Z., Li, K., Zhang, J. & Conejo, A. N. Insights into defect cluster formation in non-stoichiometric wustite ($Fe_{1-x}O$) at elevated temperatures: accurate force field from deep learning. *npj Comput. Mater.* **11**, 32 (2025).
47 Toby, B. H. & Von Dreele, R. B. GSAS-II: the genesis of a modern open-source all purpose crystallography software package. *Appl. Crystallogr.* **46**, 544-549 (2013).
48 Wei, S., Kang, J. & Tasan, C. C. An in situ synchrotron X-ray study of reverse austenitic transformation in a metastable FeMnCo alloy. *J. Mater. Res.* **38**, 281-296 (2023).
49 Kresse, G. & Furthmüller, J. Efficiency of ab-initio total energy calculations for metals and semiconductors using a plane-wave basis set. *Comput. Mater. Sci.* **6**, 15-50 (1996).
50 Kothakonda, M. *et al.* Testing the r^2SCAN Density Functional for the Thermodynamic Stability of Solids with and without a van der Waals Correction. *ACS Mater. Au* **3**, 102-111 (2022).
51 Swathilakshmi, S., Devi, R. & Sai Gautam, G. Performance of the r^2SCAN functional in transition metal oxides. *J. Chem. Theory Comput.* **19**, 4202-4215 (2023).

Supplementary Files

This is a list of supplementary files associated with this preprint. Click to download.

- SupplementaryMaterials.pdf